Experimental Mechanics (2023) 63:363–376
https://doi.org/10.1007/s11340-022-00924-9

RESEARCH PAPER

Characterization and Prediction of Polymer/Active Material Interface Failure in Battery Electrodes

A. S. Pakhare[1] · **S. P. V. Nadimpalli**[1]

Received: 5 July 2022 / Accepted: 25 October 2022 / Published online: 23 November 2022

Abstract

Background Failure of polymer/active material interfaces, in commercial composite electrodes, is one of the mechanisms by which batteries loose capacity. In spite of the importance, no systematic study to characterize and understand the interface failure behavior of battery electrodes exists at present.

Objective The objective is to develop an experimental method to characterize the fracture behavior of polymer/active material interfaces in rechargeable battery systems.

Methods Axisymmetric blister test samples were prepared by depositing PVdF (polyvinylidene fluoride) polymer on SiO_2 surface with a series of nanofabrication processes. The PVdF/SiO_2 samples were then pressurized in a novel electrochemical cell until the film delaminated from SiO_2. The mechanical response of the pressurized film was measured, and the PVdF/SiO_2 interface fracture was characterized in terms of critical energy release rate G_c. The fracture surfaces were analyzed to determine failure mechanism.

Results The X-ray photoelectron spectroscopy and scanning electron microscopy analysis of the fracture surfaces showed that the crack path was predominantly at the PVdF/SiO_2 interface, i.e., the mechanism of failure was adhesive. Hence, the measured $G_c = 2.46$ J/m^2 can be considered as the energy required to break the bonds to separate PVdF from SiO_2. Using this G_c value in a finite element model, the failure pressure of plane strain blister samples has been predicted successfully.

Conclusion We have experimentally demonstrated that G_c is a fundamental fracture parameter, and $G = G_c$ as a failure criterion can be used to predict PVdF/SiO_2 interface failure irrespective of sample geometry, which can be extended to battery electrodes.

Keywords Lithium-ion batteries · Binder-active material interface · Interface fracture · Blister test · Energy release rate

Introduction

Rechargeable batteries such as Li-ion batteries are the primary choice as energy storage devices in wide range of applications including automotive, aerospace, defense, biomedical, and clean energy production because of their high-power density and energy density. In spite of rapid advances in recent years, the capacity and cyclic life of batteries is still not sufficient to meet the growing energy demands [1]. For example, two to five times higher specific capacities and longer cyclic life than that of current batteries are necessary to meet the performance and range requirement of hybrid and all-electric vehicles for transportation applications [2].

Replacing the conventional electrode materials, e.g., graphite which has a theoretical specific capacity of 372 mAh g^{-1}, with alternative high-performance materials such as Si, Sn, and Ge can improve the capacity. For example, replacing graphite with Si, which has a theoretical specific capacity of 3579 mAh g^{-1}, can result in 30% increase in the capacity of the state-of-the art Li-ion batteries [3]. However, the high-performance anode materials suffer from poor cyclic performance and rapid capacity fade primarily due to their volume expansion behavior. For instance, Si, Sn, SiO_2, and Ge expand by more than 300% upon reacting with Li, and a recent experimental study on Na-ion electrode by Rakshit et al. [4] showed that a similar volume change behavior occurs in Na-ion electrodes. This level of deformation not only generates more than 1 GPa of stress in the

✉ S. P. V. Nadimpalli
sivan@msu.edu

[1] Department of Mechanical Engineering, Michigan State University, 48824 East Lansing, Michigan, USA

electrodes [5–8] but also applies significant strain on the polymer/active material interface causing interface fracture leading to rapid capacity fade. It should be noted that the passive layer (or solid electrolyte interphase) formation on the electrode particles is one of the capacity fade mechanisms [9–11], but here the focus is on the polymer/active material interface failure.

A strong and stable polymer/active material interface is critical not only for successful battery operation but also for longer cyclic life of a battery, because an intact interface enables the polymer binder in composite electrodes to connect all the active particles (i.e., graphite or Si in a composite electrode) and provide electrical network necessary for sustaining chemical reactions [12–17]. The electrical isolation of active particles due to polymer/active particle interface failure is one of the leading mechanisms of capacity fade [13–15, 17–19]. Studies on composite electrodes [13, 20–25] showed that a stronger bonding between binder and active particles (i.e., a stronger binder/active material interface) improved the cyclic performance of the electrodes. Similarly, in situ stress measurements in composite electrodes by Sethuraman et al. [26] and Nadimpalli et al. [23] demonstrated, experimentally, that polyvinylidene fluoride (PVdF) binder, when used in Si-based composite electrodes, showed poor cyclic performance compared to carboxymethyl cellulose (CMC), and it was attributed to the nature of bonding. Hence, understanding and characterizing the interface failure behavior is critical for improving the durability of high-performance battery electrodes.

In spite of the importance, very few studies [13, 22–25, 27, 28] exist on the binder/active material interface failure and all of them are qualitative in nature. For example, scratch tests [27, 29], and peel test [21, 28, 30] can only provide relative ranking of interface strength and do not measure fundamental mechanical properties that can be used to predict the failure of the interfaces under other configurations or loading conditions. More recently, Ebner et al. [31] and Muller et al. [32] carried out X-ray imaging of composite electrodes to understand the interface degradation mechanisms. However, a systematic study on the direct measurement of fundamental mechanical property that characterizes the interface failure in battery electrodes is still missing. The challenges associated with measurements on micro or nanoscale samples (typical dimension of binder bridges in composite electrodes) and the lack of mechanical characterization of active materials [5, 7, 33, 34] and polymer binders [13, 16, 22, 24, 25], until recently, could be one reason for the lack of systematic study on the interface failure characterization.

The objective of this study was to develop an experimental method to characterize the fracture behavior of polymer/active material interfaces in rechargeable (Li-ion and beyond Li-ion) battery systems. To this end, an optical setup based on Michelson interferometer principle has been designed and fabricated; a sample that mimics the interfaces in commercial battery electrodes and a novel electrochemical cell have been designed. The conventional and most widely used polymer binder, polyvinylidene fluoride (PVdF), and SiO_2 as active material was chosen as a model system for interface fracture characterization due to their practical importance. The mechanical behavior of the free standing PVdF film on SiO_2 substrate was characterized thoroughly and analyzed using analytical and finite element methods. The PVdF/SiO_2 interface fracture was characterized in terms of critical energy release rate G_c by using axisymmetric (circular) sample in a blister test method. Using the measured G_c as a failure criterion, failure behavior of pressurized rectangular plane strain membrane has been predicted. It should be noted that despite the challenges associated with the diffusive surface characteristics and transparency of PVdF films, for the first time, the PVdF/SiO_2 interface fracture has been characterized in terms of critical strain energy release rate successfully. This study lays the foundation for fundamental understanding of binder/active material interface failure in rechargeable batteries. Characterizing the interface failure in terms of energy release rate brings the robust thermodynamic framework of fracture mechanics into multiphysics battery models, i.e., to simulate interface degradation behavior of electrodes.

Experimental Methods

PVdF-SiO_2 Sample Preparation

Figure 1(a) shows a schematic of the interface fracture sample which consists of a uniform thin film of PVdF bonded to SiO_2 surface, and the schematic in Fig. 1(b) shows a sequence of micro and nanofabrication processes used to fabricate the samples. An optical micrograph of the actual (axisymmetric or circular) sample is shown in Fig. 1(c). First, a single side polished Si wafer (4 in diameter, 550 µm thickness) with a 500 nm of thermally grown SiO_2 layer was rinsed with acetone and isopropyl alcohol to remove any contaminants on the surface. Using a standard photolithography process (Karl Suss MA/BA6 mask aligner) and SPR220 photoresist (Megaposit™), a circular (1000 µm diameter) pattern was created on the rough side of the wafer. The exposed circular areas of SiO_2 were etched using inductively coupled plasma-reactive ion etching (ICP-RIE, SPTS Technologies) to remove the oxide; this was followed by through etching of Si using deep reactive ion etching (DRIE, SPTS Technologies) to create the trench below free-standing area of the film. After these etching steps, the samples were thoroughly cleaned with acetone, isopropyl alcohol, and nanostrip (a stabilized mixture of sulfuric acid and hydrogen

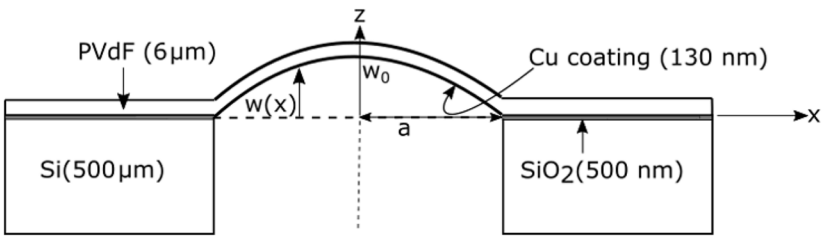

(a)

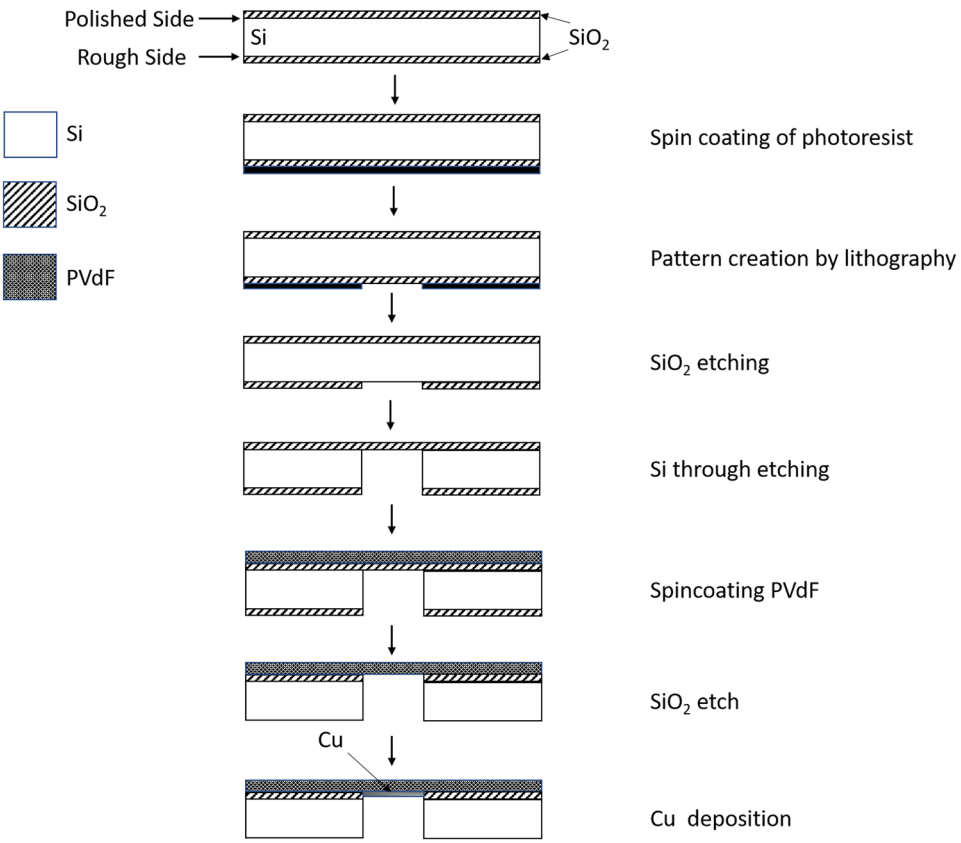

(b)

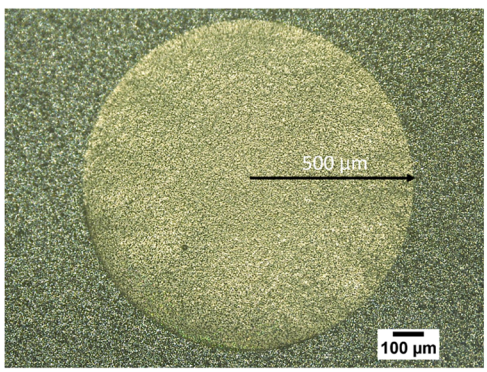

(c)

Fig. 1 (**a**) Schematic of the cross section view of PVdF/SiO_2 sample showing geometric details, various system parameters, and the coordinate system that will be used throughout the paper, (**b**) the sequence of steps in sample preparation process, and (**c**) a micrograph of the axisymmetric sample with 1000 μm diameter used for PVdF/SiO_2 interface fracture property G_c measurement

peroxide) to remove any organic residue on surface of SiO_2 (on the polished side of the wafer) that will be bonded to PVdF.

A uniform solution of 10 wt% PVdF in NMP (1-Methyl-2-pyrrolidone) was spin coated on the free-standing SiO_2 surface at 600 rpm for 30 s using a spin coater (VTC-100 A, MTI Corp.) and dried at 100 °C for 1 h to obtain a 6.0 ± 1.0 μm PVdF film on the SiO_2 surface. The free standing SiO_2 film supporting the PVdF was removed using reactive ion etch (or RIE etch, Nordson March RIE-1701) to create a free standing PVdF film as shown in Fig. 1(c). Since the PVdF film is translucent, a 130 nm Cu was sputter deposited on the lower surface of PVdF, also seen in Fig. 1(c), to enable light reflection and optical measurements.

Experimental Setup and Test Procedure

Figure 2(a) shows the schematic of the experimental setup which consists of four components: (1) blister test cell, (2) pressure transducer, (3) mass flow controller, and (4) an interferometer. All these components are controlled and monitored by a computer via a LabView program; the program controls the sensors, records the data, acquires images, and synchronizes the data with images obtained during fracture test. The samples (prepared as per Fig. 1) were placed in the custom-made blister test cell and clamped with gaskets above and below the sample to prevent leak. The current cell design and clamping method produced a leak free cell up to a pressure of 250 kPa (as shown in Fig. S1), which is significantly higher than the critical pressures expected in the current experiments.

After assembling the cell and clamping the sample, the free standing PVdF film was pressurized using ultra-high purity Ar gas through an orifice located below the freestanding film area as shown in Fig. 2(a). A constant mass flow rate of 0.8 cm^3/min (SCCM) or 1.33×10^{-9} m^3/s of Ar gas was maintained throughout the test using a mass flow controller (Alicat MC-1SCCM-D) which can control the flowrate to within 1% of the setpoint value. This mass flowrate resulted in a constant 0.43 kPa/min of pressure loading on the PVdF film during the test. The pressure in the test cell chamber was measured using a pressure sensor (Omega PX309-050a5v) with a resolution of ~1 kPa. The pressure on the film was increased monotonically until the film completely delaminated from the SiO_2 surface. Images of the pressurized film were captured (using an optical system with a ~5 μm spatial resolution) at an interval of 400 ms throughout the test. The pressure value corresponding to a 50 μm (of crack) delamination is considered as the crack initiation pressure (P_c). Figure 3(b) shows an example of a sample with significant delamination. For clarity, a portion of the boundary between intact region and delaminated region is highlighted with a dotted line. Since, the mechanical properties (including the adhesive properties) may change with temperature, all the experiments were conducted at room temperature under isothermal conditions.

In addition to pressure, the deflection profile of the PVdF film was measured during the test using the interferometer setup that was designed and fabricated in-house. The setup is based on the Michelson interferometry principle and Fig. 2(b) shows the details of the interferometer. A green light spectrum with 550 nm ± 10 nm wavelength

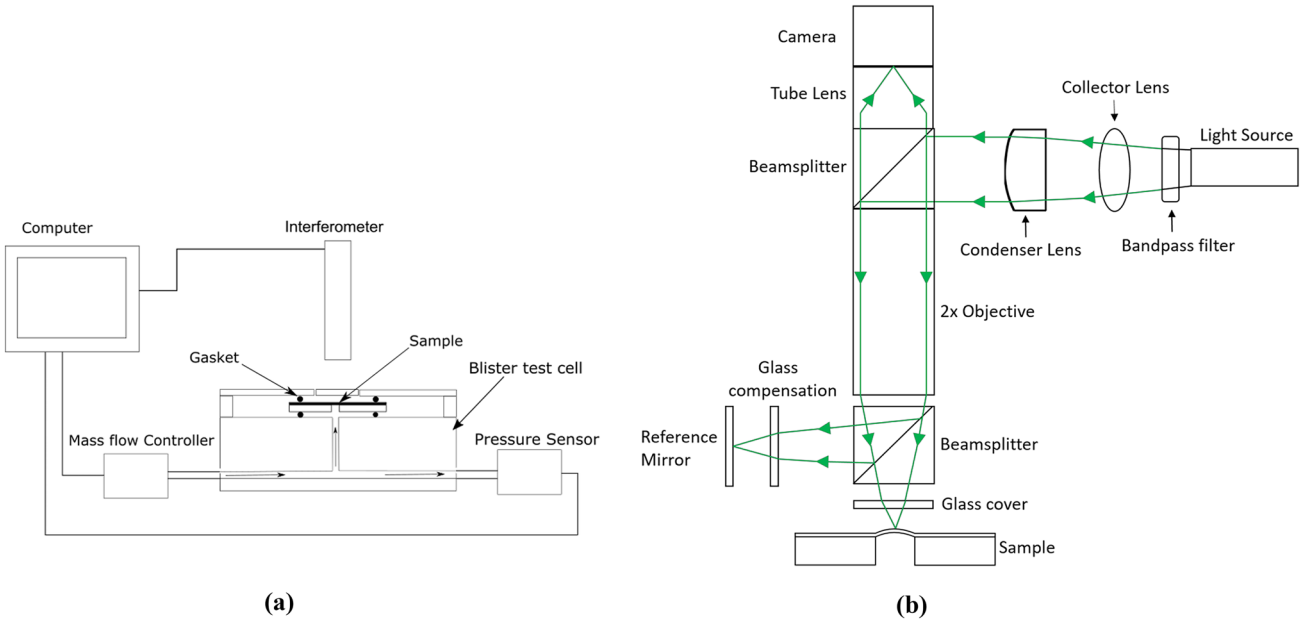

Fig. 2 (**a**) Schematic of the experimental setup used for characterization of binder/active material interface fracture, and (**b**) the details of the interferometer used for the measurement of out-of-plane displacements of pressurized PVdF film. The synchronization of data from the pressure transducer and images from the camera enable identification of the critical pressure at the onset of delamination

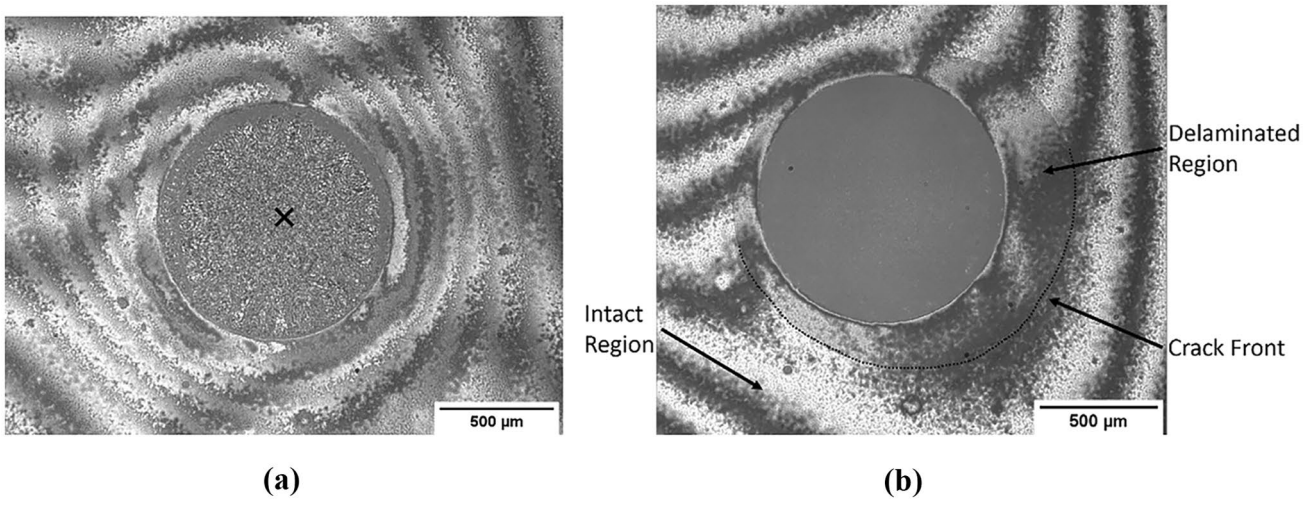

Fig. 3 (**a**) An axisymmetric sample with typical interference pattern formed on the surface is shown prior to delamination, and the symbol 'x' indicates a pixel (at the center of the circular region) chosen for further analysis. (**b**) A sample after some delamination of PVdF from SiO_2 surface is shown, where a portion of delamination/crack front is highlighted with a dotted-line for clarity

was employed, and it was obtained by passing white light through a bandpass filter. A combination of collector lens and condenser lens was used to produce a collimated beam of green light (whose light ray remains parallel) and an even illumination of the sample. A beam splitter directs the collimated beam towards a 2x Mitutoyo objective as shown in Fig. 2(b). The objective was selected to have a field of view big enough to see the full sample and have enough working distance to accommodate optical and sample clamping components. A second beam splitter, located between the objective and the sample, splits the light beam into two and directs one towards a fixed reference mirror and the other towards the sample surface. The reflected beams from the sample and the fixed standard (flat) mirror create an interference pattern due to the slight variations in the optical path lengths travelled by the two beams. Figure 3(a) shows typical interference patterns formed on an axisymmetric sample. The images of the interference pattern are recorded using a CMOS-based monochromatic camera (2MP Basler ace, Edmund Optics Inc.). As the coherency length of the light used is small, it would be difficult to produce interference pattern if the optical path lengths of the beams (travelling from sample surface and the standard mirror) deviate significantly. As a result, a glass window was placed at the reference mirror (Fig. 2(b)) with the same thickness and refractive index as that of the window near the sample surface to balance the optical path lengths.

The displacement profile of the pressurized PVdF film was obtained by analyzing the interference patterns recorded at a regular interval of 400 ms during a test. A typical interference pattern formed on the samples can be seen in Fig. 3(a). The passage of each fringe (i.e., the center of one bright (dark) fringe to the next bright (dark) fringe) is equal to 275 nm of an out-of-plane displacement of sample surface, i.e., half of the wavelength of the green light used in the setup (i.e., Fig. 2(b)). Hence, in principle, the height profile of the sample surface or pressurized PVdF film at any given time can be obtained by simply counting the number of fringes from the edge of the free-standing area to the center. Such a fringe counting method has been previously used to obtain out-of-plane displacements [35–38], and it works well for specularly reflective surfaces for which fringe patterns are clear and regular (such as the PVdF/SiO_2 interface in Fig. 3(a)). However, rough diffuse surfaces might complicate the fringe counting method; for example, the fringe pattern formed on free-standing PVdF area (i.e., the circular region in the middle of Fig. 3(a)) is not well defined. Hence, fringe counting method to obtain spatial displacement profile is relatively more challenging.

Due to this challenge, a slightly modified method was implemented to analyze the fringe patterns to obtain the displacement profile of the pressurized PVdF film. Instead of counting number of fringes formed on the entire surface area of the free-standing PVdF film, number of fringes passing a given point on the sample was counted. For example, the intensity of each pixel such as the one indicated with "x" in Fig. 3(a) was obtained as a function of time throughout the test by analyzing all the images of a particular test with an image processing code written in Matlab software [39]. Figure 4 shows the normalized intensity as a function of time of the pixel (or the point) indicated as "x" in Fig. 3(a). The normalized intensity is the ratio of intensity recorded to the maximum intensity (which for an 8-bit image is 256). The intensity reaches a peak every time a fringe passes the point;

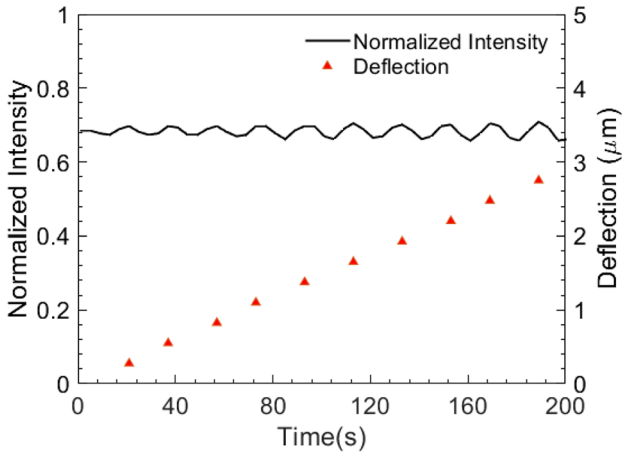

Fig. 4 Intensity of the pixel (or point) indicated as 'x' in Fig. 3(a) is plotted as a function of time during the experiment. The triangle symbol (corresponding to intensity peaks) represents the out-of-plane deflection of the point 'x' as a function of time. In this example, the total out-of-plane displacement is ~2.75 μm (as 10 peaks passed the point in 200 s)

hence, the number of peaks in Fig. 4 represent the number of fringes that passed the point 'x' in 200 s, which is equal to an out-of-plane displacement of ~2.75 μm (i.e., 10×275 nm). The filled triangle symbol represents the out-of-plane displacement of the point 'x' as function of time. It should be noted that the resolution of the system shown in Fig. 2 is $\lambda/4$ =137.5 nm, i.e., peak to valley distance in Fig. 4. With this procedure, one can obtain out-of-plane displacement of each point on the sample surface during the experiment, even if there are no well-defined and clearly identifiable fringes as seen on the free-standing PVdF surface Fig. 3(a), i.e., on the circular area.

Theoretical Methods

Finite element analysis

Abaqus finite element (FE) software [40] was used to simulate the mechanical behavior of pressurized PVdF film and the PVdF/SiO_2 interface fracture. It should be noted that the deformation behavior of pressurized films consists of small strain but large rotations [41]; hence, NLGEOM ON option in Abaqus that simulates the large deformation kinematics was prescribed. Figure 5 shows the finite element mesh (of sample in Fig. 1) along with the boundary conditions of the PVdF film on SiO_2. The substrate was fixed by constraining nodes on the bottom surface. A symmetric displacement boundary condition was prescribed for the nodes on the left edge of the film at x = 0 μm. The thickness of the substrate does not affect the stresses either in the PVdF film or at the PVdF/SiO_2 interface, hence, it was adjusted to 100 μm to optimize computation time. Similarly, the stresses in PVdF film, in SiO_2, or at the interface far from the crack tip in the radial distance tend to be negligible (as shown in Fig. S2); hence, only a portion of the sample dimension was modeled.

The PVdF film was discretized with 8-noded quadrilateral elements CAX8R, and at least ten elements were included across the thickness of the film with the smallest element size being 125 nm. As per the sample, a Cu coating of 130 nm below the free-standing PVdF was included in the model. Similar to PVdF, the SiO_2 and Si was discretized with CAX8R elements, with the size of smallest element being 125 nm. As per the experiments, a 50 μm crack was modeled at the interface, and to capture the stress singularity, the region around the crack tip, i.e., the first ring of elements shown within the circle around crack tip in the inset of Fig. 5, is modeled using special 6-noded triangular elements called singularity elements formed by collapsing 3 nodes of 8 node CAX8R element. The mesh grading and the element sizes in Fig. 5 were optimized through mesh sensitivity study, and further reduction in element size did not produce any significant change in the results. The strain energy release rate was obtained by evaluating contour integral (or J-integral) around the crack tip. The method involves defining the crack tip, crack flanks, and the direction of crack growth as shown in the inset of Fig. 5. The J-integral [42, 43] was evaluated for several contours sufficiently far from the crack tip, to ensure that the evaluated J-integral values are path independent. Since the crack is at the interface, besides the energy release rate, one has to evaluate the

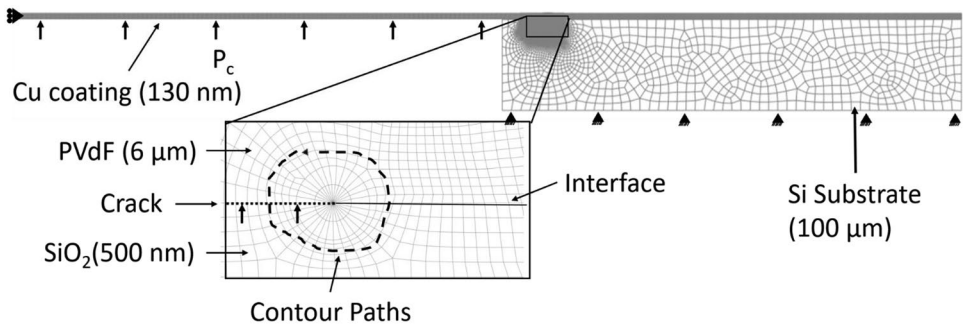

Fig. 5 Finite element mesh and boundary conditions of the blister test sample. The inset shows the mesh details near the crack tip and a typical contour used to evaluate J-integral. The J-integral (or energy release rate) was evaluated for the crack initiation pressure obtained from experiments

phase angle which provides a measure of shear to opening stresses near the crack tip. The phase angle is given by $\psi = \tan^{-1}\left(\sqrt{\frac{G_{II}}{G_I}}\right)$ where G_I and G_{II} are the energy release rates corresponding to opening and shear mode of fracture, respectively. I. S. Raju [44] proposed a virtual crack closure technique (VCCT) for 6-noded singularity elements to calculate energy release rate and corresponding phase angle for linear elastic materials; the method was implemented for axisymmetric elements by Figiel and Lauke [45]. This method was used here to determine the phase angle and to verify if the energy release rate obtained from VCCT matches with that obtained from J-integral.

The PVdF polymer was modeled as a rate dependent isotropic hardening model with the flow rule given as,

$$\dot{\bar{e}}^{p} = D\left(\frac{\bar{\sigma}}{\sigma^{0}} - 1\right)^{n}, \tag{1}$$

where $\dot{\bar{e}}^{p}$ is the equivalent plastic strain rate, D and n the temperature dependent material parameters, σ^0 the static yield stress, and $\bar{\sigma} = \sqrt{\frac{3}{2}\mathbf{S}:\mathbf{S}}$ the equivalent stress, where $\mathbf{S}$ is the deviatoric stress tensor. As the experiments were conducted under isothermal conditions, no temperature dependence is considered in the model. The experimental true-stress and true-strain data of PVdF from Santimetaneedol et al. [24] was provided directly as input to the model. The SiO_2, Si, and Cu coating are modeled as linear elastic materials. The elastic properties of these materials are outlined in Table 1.

Analytical methods

The deformation response and fracture parameters of the pressurized films were also evaluated using closed form analytical expressions proposed in the literature. Although PVdF exhibits time-dependent material behavior [24], it was assumed as linear elastic material to ascertain if this simple model can capture the mechanical behavior of the film prior to the onset of delamination. When the deflections of the film increase to values on the order of film thickness, as in PVdF films here, the films behave more like a membrane [41]. Using the membrane theory assumption, Small et al. [47] derived the pressure - central deflection relation for pressurized circular membranes as,

$$P = C_1\frac{\sigma_R t_c}{a^2}w_0 + C_2\frac{E_c t_c}{(1-\nu)a^4}w_0^3, \tag{2}$$

where, P is the pressure applied and $w_0 = w_i + w_m$ the central deflection as per Fig. 1. Here the central deflection (w_0) is sum of the initial height (w_i) for non-flat films and measured deflection (w_m). The geometric parameters of the sample are: the radius of the free-standing film a, the film thickness t_c, and the geometry dependent constants C_1 and C_2 are 4 and 2.475 [38, 47], respectively, for a circular membrane. Since these equations are for linear elastic membrane, the necessary material properties are E_c the Young's modulus of the film and υ the Poisson ratio. The σ_R is the residual stress.

Since a layer of Cu is deposited below PVdF, the elastic modulus of the PVdF/Cu composite film is obtained by following the method proposed by Small et al. [48]. The biaxial modulus of the composite film is obtained as

$$M_c = \frac{t_f}{t_c}M_f + \frac{t_{Cu}}{t_c}M_{Cu} \tag{3}$$

where, M is biaxial modulus and the subscripts *f, Cu*, and *c* refer to PVdF film, Cu and composite, respectively. The t_f, t_{Cu}, and $t_c = (t_f + t_{Cu})$ are the thickness of PVdF, Cu, and composite, respectively. Since Poisson's ratio of PVdF and Cu are similar referring to Table 1, the Young's modulus of composite film was determined to be 4.1 GPa by using M_c value from (equation (3)) in $E_c = M_c\ (1 - \nu)$. The corresponding energy release rate for pressurized circular membrane [38] is given as,

$$G = \frac{5}{8}C_2\frac{E_c t_c {w_0}^4}{a^4} \tag{4}$$

The G_c can be evaluated analytically by substituting the central deflection w_0 corresponding to the onset of crack growth and other parameters in (equation (4)). The critical w_0 corresponding to the critical pressure P_c can be obtained by solving the (equation (2)) using the Newton-Rhapson method.

Table 1 Mechanical properties of materials used in the finite element simulation

Material	Parameter	Values	References
SiO_2	Young's Modulus	71 GPa	[41]
	Poisson Ratio	0.16	
Cu	Young's Modulus	130 GPa	[41]
	Poisson Ratio	0.34	
Si	Young's Modulus	160 GPa	[46]
	Poisson Ration	0.28	

Results and Discussion

Characterization of PVdF/SiO_2 Interface Failure

Mechanical response and crack-tip conditions

The mechanical response of a pressurized film is a function of the initial height w_i, film thickness t_c, mechanical

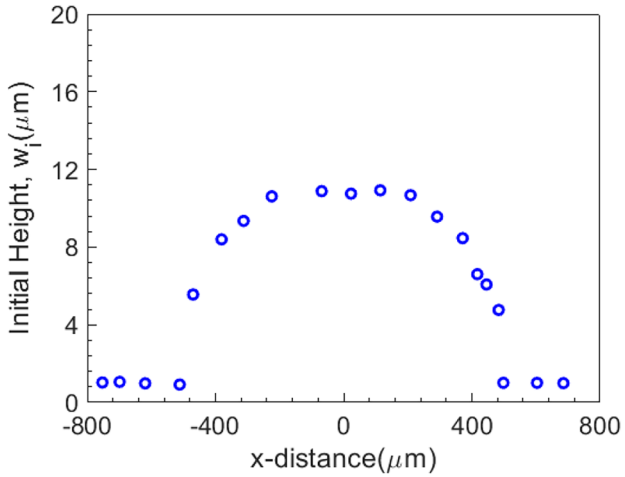
Initial Height, $w_i(\mu m)$
x-distance(μm)
20
16
12
8
4
0
-800
-400
0
400
800

(a)

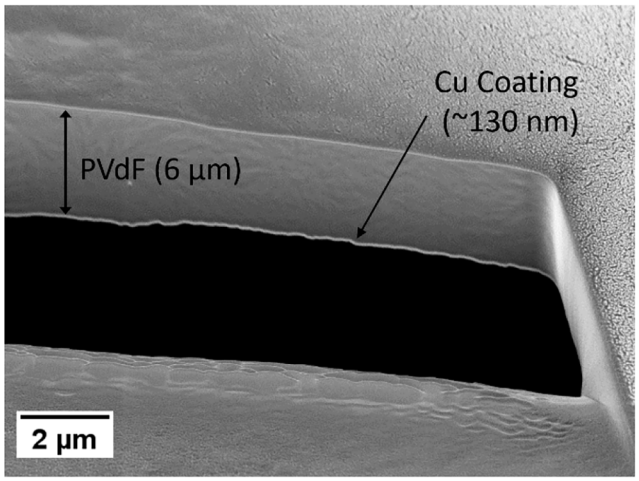
Cu Coating
(~130 nm)
PVdF (6 µm)
2 µm

(b)

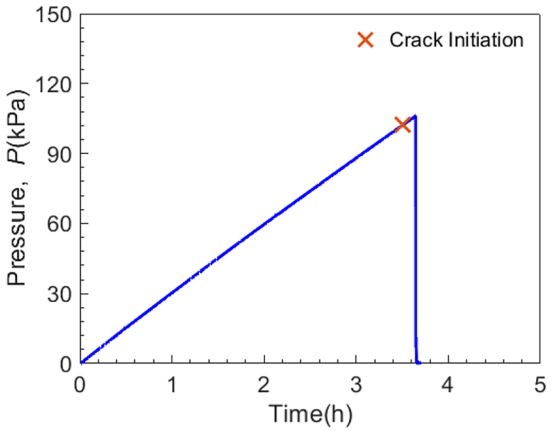
Crack Initiation
Pressure, P(kPa)
Time(h)
150
120
90
60
30
0
0
1
2
3
4
5

(c)

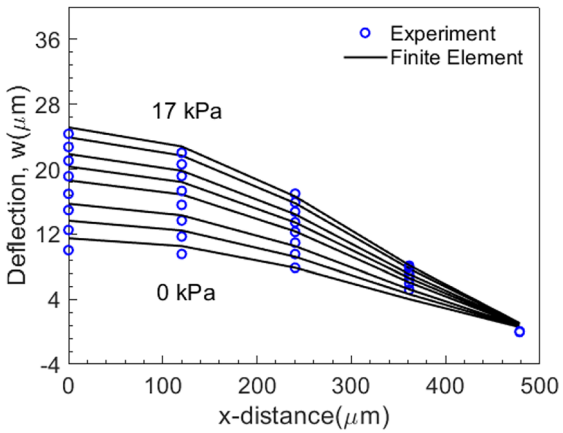
Experiment
Finite Element
17 kPa
0 kPa
Deflection, w(μm)
x-distance(μm)
36
28
20
12
4
-4
0
100
200
300
400
500

(d)

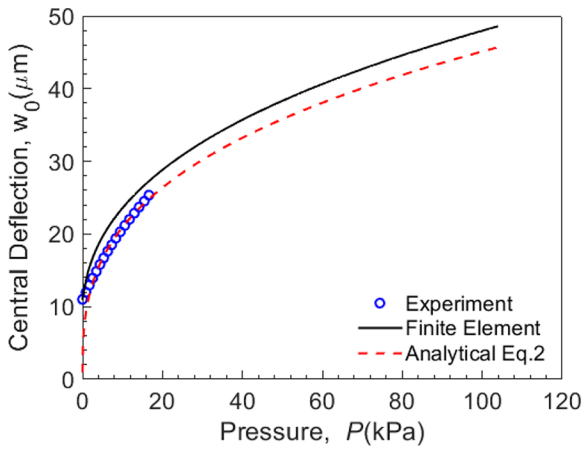
Experiment
Finite Element
Analytical Eq.2
Central Deflection, $w_0(\mu m)$
Pressure, P(kPa)
50
40
30
20
10
0
0
20
40
60
80
100
120

(e)

◂**Fig. 6** (**a**) The profile of circular PVdF film measured under zero applied pressure, (**b**) the cross section of free-standing PVdF film obtained by FIB milling, (**c**) prescribed pressure loading on the film (the critical pressure associated with onset of delamination is indicated with "x"), (d) comparison of experimentally measured film profiles at various levels of pressure with those obtained from finite element analysis, and (**e**) comparison of pressure-central deflection response (p-w_o) of the film measured from experiments and those obtained from analytical and finite element models

properties, and residual stress σ_R. Hence, it is important to measure these parameters to characterize the mechanical behavior of the PVdF film and PVdF/SiO_2 interface failure. Figure 6(a) shows the typical profile of a free-standing circular PVdF film measured (using Zygo NewView5000 optical profilometer) before pressurizing the film. Note that the film is not flat at the start of the experiment, i.e., under zero applied pressure, and this is true in all the samples tested here. This is expected because (during the sample preparation process, Fig. 1(b)) the thermally grown SiO_2 film releases its compressive residual stress by buckling out-of-plane when the substrate is etched away; this out-of-plane buckling is inherent to SiO_2 films [49]. The spincoated PVdF film assumes the shape of the relaxed out-of-plane buckled configuration of SiO_2, resulting in the profile shown in Fig. 6(a).

Figure 6(b) shows the cross-section image of the free-standing PVdF film obtained using FIB (focused ion beam) milling method. This shows that the thickness of the free-standing PVdF film is ~6 μm which matches with the thickness of the PVdF film measured far from the free-standing area, providing confirmation that the sample processing steps (etching processes shown in Fig. 1) did not alter the film thickness. However, the PVdF/Cu interface, which primarily contributes to the light reflection and interference pattern formation in the free-standing area, became relatively rough compared to PVdF/SiO_2 interface. This explains the reason why the interference patterns in the free-standing area are not well defined when compared to those from PVdF/SiO_2 surface in Fig. 3. The residual stress σ_R in the film not only affects the mechanical behavior but also affects the delamination behavior of the PVdF film [50, 51]. Using a Multibeam optical sensor (MOS) setup shown in Fig. S3 the residual stress in PVdF thin film on SiO_2 was measured and it was ~3 MPa tensile stress (Fig. S3).

Figure 6(c) and (d) show the prescribed pressure loading and the evolution of the film profile at various levels of pressure, respectively. The critical pressure at the onset of film delamination is indicated with a symbol 'x'. The open circle symbols in Fig. 6(d) represent the experimental data and the solid curves represent FE results. The deflection-pressure data corresponding to x = 0 μm from Fig. 6(d), i.e., at the center of free-standing film, is plotted in Fig. 6(e), which is commonly referred to as pressure-central deflection response (p-w_o) of the PVdF film. Although pressure is monitored and recorded continuously throughout the experiment, the displacement data is available only until about 30 μm, due to the characteristic bandwidth of green light source used here. Note from Fig. 6(d) and (e) that there is an excellent agreement between experimentally measured deflections and film profile at various levels of pressure and the corresponding FE data; in other words, the overall mechanical behavior of the PVdF film on SiO_2 was captured very well by the finite element model. This could be attributed to the fact that in addition to an accurate constitutive model of PVdF, all the critical system parameters discussed above, i.e., thickness, initial profile, and residual stress of the PVdF film have been accounted for in the FE models. The initial (non-flat) profile of the film, i.e., Fig. 6(a), under zero pressure, was included in FE analysis by first deforming the mesh until the profile matched experimental values in Fig. 6(a) and then importing the deformed mesh as the starting geometry for the subsequent simulation, where pressure-time loading shown in Fig. 6(c) was prescribed along with the boundary conditions shown in Fig. 5. The residual stress in the film was included in the simulation as an initial condition.

It is interesting to note from Fig. 6(e) that the pressure-central deflection, i.e., $(p - w_0)$ response predicted by the analytical solution i.e., (equations (2) and (3)), (dashed line) also matches very well with the experimental data. This is interesting because the analytical equation is based on the theory of linear elasticity, yet it predicts the mechanical response of the elastic-viscoplastic PVdF film successfully. This can be explained by looking at the stress and strain fields in the PVdF film. Figure 7 shows the von Mises equivalent stress and equivalent plastic strain contours of PVdF film at the onset of crack growth (i.e., at the critical pressure). Note that the equivalent stress near the center of the circular membrane (i.e., in the central deflection region, inset on the left side in Fig. 7) is between 12 and 24 MPa which is below the yield strength of PVdF reported by Santimetaneedol et al. [24], and the equivalent plastic strain contour (inset on the right side in Fig. 7) shows that the plastic deformation of PVdF film occurs in a very small region surrounding the crack tip. As a result, the deformation of PVdF film is nominally elastic prior to the onset of crack growth, which explains why the analytical solution was able to predict the mechanical behavior of PVdF film reasonably well. This is analogous to small scale yielding condition in linear elastic fracture mechanics theory which justifies the application of linear elastic theory to ductile materials such as steel for example [42, 43]. Thus, the current experimental setup and testing method ensure nominally elastic conditions prior to the onset of delamination which enables the interface fracture characterization with simple linear elastic properties of PVdF film and corresponding analytical solutions.

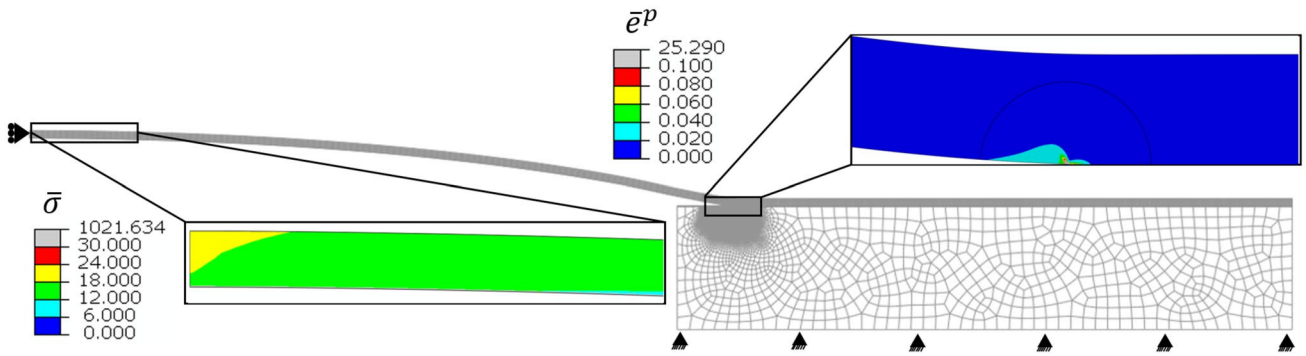

Fig. 7 Deformed mesh of the circular membrane at the critical pressure is shown along with the equivalent (von Mises) stress $\bar{\sigma}$ contour near the center of the film (inset on the left side) and the equivalent plastic strain $\bar{e}^p$ contour near the crack tip (inset on the right side). This confirms that the PVdF film remains nominally elastic prior to onset of delamination, i.e., existence of small-scale yielding conditions

PVdF/SiO_2 interface fracture behavior

The critical pressure at the onset of crack propagation measured from circular blister tests is used in FE models to determine the critical energy release rate G_c of PVdF/SiO_2 interface and is shown in Table 2. It should be noted that, to measure the linear elastic fracture property, i.e., the interface fracture energy G_c, it is extremely important to ensure that the dissipative mechanisms such as plastic deformation are limited to a very small region near the crack-tip in a fracture sample as shown in Fig. 7. The maximum, minimum, and the average critical energy release rate G_c values of PVdF/SiO_2 interface are 3.04 J m^{-2}, 2.02 J m^{-2}, and 2.46 J m^{-2}, respectively. As expected, due to the small-scale yielding conditions in the samples, the G_c evaluated from analytical equations matched very well with the FE calculations. Although the analytical equation assumes a flat PVdF film under zero applied pressure, the G_c matched with the comprehensive FE model; hence, the errors associated with an initial non-flat film profile may be negligible for PVdF films.

In order to understand the potential errors in measured G_c due to the uncertainty associated with the PVdF/SiO_2 sample parameters, several finite element simulations were conducted. It was observed that if the initial profile of the film was neglected (i.e., if the free-standing film was assumed to be flat), keeping everything else constant, the error in G_c will be 0.03%, i.e., negligible. This is why the analytical data (with flat film assumption) matched with FE data very well. The reason for this can be evident from Fig. 6(e), where the central deflection of the film rises steeply to ~ 12 µm with negligible pressure; hence, as long as the initial height of the film is less than 12 µm, error associate with neglecting initial height of the film is minor. However, neglecting the residual stress σ_R, on the other hand, will lead to an overestimation of the G_c by 7%. If both the initial profile and residual stress in the film are neglected, then G_c will be overestimated by 8%. Since the initial height and residual stress, film thickness, radius of the film, and critical pressure were measured experimentally, the variation in the G_c values presented are primarily due to the sample to sample variation.

Figure 8 shows the fracture surface of the sample after the PVdF film was completely delaminated from the SiO_2 surface. To understand the crack path and fracture mechanism, an X-ray photoelectron spectroscopy (XPS) analysis was performed on the fracture surface (shown in Fig. 8), and the results are compared in Table 3 with that of bare SiO_2 and pure PVdF film. Note that the elemental composition, except for the fluorine, of the fractured surface resembles

Table 2 The critical pressure at the onset of delamination and the corresponding critical energy release rate G_c values of PVdF/SiO_2 interface measured from seven circular blister tests. The phase angle ψ corresponding to these measurements is 41°. The FE model is comprehensive and closely represents the actual experimental conditions. Although the analytical method assumes the film as linear elastic and flat under zero applied pressure, the solution matched very well with that of FE model since the initial height is not a critical parameter and the small-scale yielding condition existed in these samples

Sample	Crack Initiation Pressure (kPa)	Critical Energy Release Rate G_c (J m^{-2}) of PVdF/SiO_2 interface	
		Finite Element Model	Analytical (equation (4))
Sample 1	106	3.04	3.18
Sample 2	104	2.92	3.06
Sample 3	81	2.04	2.09
Sample 4	91	2.45	2.55
Sample 5	90	2.47	2.52
Sample 6	80	2.02	2.04
Sample 7	87	2.28	2.36
Mean ± standard deviation	**91 ± 10**	**2.46 ± 0.40**	**2.54 ± 0.44**

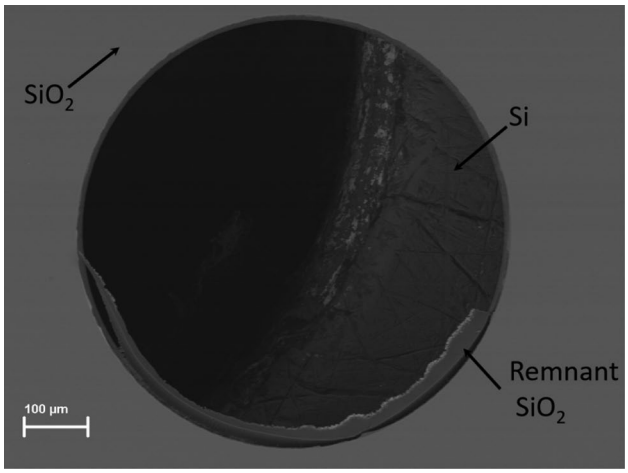

Fig. 8 Scanning electron microscope backscatter image of the fracture surface (i.e., surface after free standing PVdF delaminated from SiO_2). The table shows the atomic weight fractions of elemental C, O, F, and Si obtained from the XPS analysis showing nearly identical stoichiometry of bare SiO_2 and delaminated region (with some fluorine on the surface)

that of bare SiO_2 surface quite closely, confirming that the crack propagation occurred between PVdF/SiO_2 interface and not in the PVdF film or in the SiO_2 substrate. Hence, the mechanism is predominantly adhesive failure (i.e., delamination of PVdF film from SiO_2) rather than cohesive (i.e., failure of PVdF film). Since the film was nominally elastic until the onset of crack growth, the measured G_c values characterize the resistance of PVdF/SiO_2 interface to delamination, i.e., the energy necessary to break bonds between PVdF and SiO_2. If the crack propagation occurs primarily in PVdF (i.e., the mechanism becomes cohesive), the energy required to propagate the crack will be higher. As the G_c values presented in Table 2 are fundamental fracture properties, they can be used in predicting the failure of PVdF/SiO_2 interface systems, irrespective of the electrode geometry (i.e., thin film, particles, nanotubes etc.). Although our samples showed predominantly interface failure, it should be noted that several possible crack propagation paths exist in a composite electrode. For example, depending on the fracture resistance of the material, crack can propagate in the polymer binder, in the active material, or at the interface. Hence, for a comprehensive understanding of electrode degradation, in addition to fracture properties of the interface,

Table 3 Composition of elemental C, O, F, and Si on various surfaces

Sample/Composition (at%)	C	O	F	Si
Bare SiO_2	22.37	44.77	0.00	32.86
PVdF	63.23	0.00	36.77	0.00
Fractured Surface (Fig. 8)	20.17	40.54	7.46	31.83

it is also important to understand the fracture properties of the materials adjacent to the interface.

When a crack propagates at an interface between two dissimilar materials (i.e., similar to PVdF and SiO_2 in Fig. 8), even a pure tensile remote load leads to a mixed-mode fracture [42, 43, 52]. Depending on the nature of interface and the adjoining solids, the fracture energy G_c of an interface could be a strong or weak function of the mode-mixity [53, 54]. The degree of mode-mixity is generally characterized by the phase angle ψ which provides a relative ratio of shear to tensile load on a crack tip. The phase angle ψ of the PVdF/SiO_2 interface in the blister test samples was evaluated using the virtual crack growth technique (VCCT) [44, 55], and it was 41°. Since the crack growth occurred at the PVdF/SiO_2 interface in all the samples tested here, the fracture energy presented in the Table 2 should be associated with a phase angle of 41° for PVdF/SiO_2 system.

G_c as Fracture Criterion to Predict PVdF/SiO_2 Interface Failure

To experimentally validate and demonstrate the predictive capability of the fracture criterion $G = G_c$, samples with a rectangular PVdF film on SiO_2 surface, as shown in Fig. 9(a), were pressurized until failure, and the critical pressure of failure was recorded. Figure 9(b) shows the comparison of critical pressure obtained from experimental measurements and finite element fracture analysis using the average $G_c = 2.46\ \mathrm{J\ m^{-2}}$ measured from circular blister samples presented in Table 2. The finite element mesh of the rectangular plane strain sample shown in Fig. 9(a) was created in Abaqus following a similar procedure outlined in "Finite Element Analysis" section. The PVdF film was modeled as elastic-viscoplastic material with continuum plane strain elements (CPE8R). The residual stress in the PVdF film and the initial profile of plane strain sample (Fig. S4), recorded using Zygo NewView5000, were considered in the FE analysis.

Note from Fig. 9(b) that the failure pressure predicted by the finite element model matched reasonably well the experimental measurements in five different samples. The slight difference in the measured and predicted pressure values in Fig. 9 can be attributed to the fact that an average G_c was used in the predictions and the phase angle of the plane strain samples at failure is 46° which is slightly different from the circular blister samples. Since the average value of measured G_c was used to predict failure, the average or the mean failure pressure was predicted remarkably well. This prediction verifies that the measured energy release rate G_c (presented in Table 2) is independent of geometry and supports our argument that G_c is a fundamental fracture property of the binder/active material interface and can be used in the battery models to predict mechanical degradation of electrodes. It is important to note that G_c, in general, is a

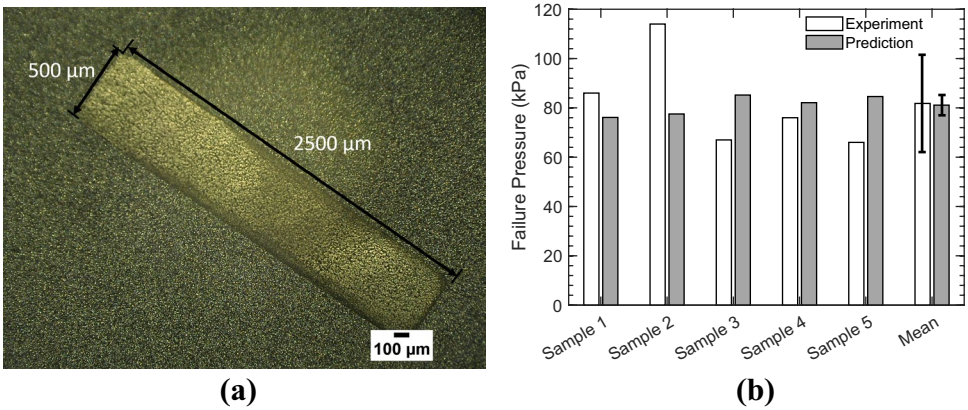

Fig. 9 (**a**) Rectangular PVdF film sample prepared following the fabrication process outlined above, (**b**) bar chart showing the experimental failure pressure from 5 samples and their average along with predicted failure pressure using $G = G_c$ as failure criterion

function of ψ; hence, measuring G_c for a range of practically relevant phase angles ψ will improve not only the accuracy of failure predictions but also the utility of fracture criterion. The ability to predict the binder/active material interface failure, as demonstrated above, will be a useful tool for battery engineers in designing durable battery electrodes.

Conclusion

An experimental methodology to characterize the failure behavior of binder/active material interfaces in battery electrodes is established using PVdF/SiO_2 as a model interface. A blister test sample that mimics the PVdF/SiO_2 interfaces in commercial batteries was fabricated using a series of nanofabrication processes. The samples were then assembled in a cell to pressurize the PVdF film until it delaminates from the SiO_2 surface. The pressure and deflection behavior of the film was measured during the experiment; an in-house built Michelson interferometer was used to measure film deflections.

The critical pressure measured at the onset of crack propagation was then used in a finite element model to evaluate the critical strain energy release rate G_c of the PVdF/SiO_2 interface. The FE model accurately accounted for all the experimental conditions including the initial profile of the PVdF film (which was not flat under zero applied pressure) and the residual stress in the film which was measured (to be ~3 MPa) using a well-known substrate curvature measurement technique. The sample design and current testing method ensured small-scale yielding conditions in the PVdF/SiO_2 sample, i.e., the sample was nominally elastic throughout the test, and the plastic deformation of the PVdF was confined to a very small region near the crack tip. As a result, the critical energy release rate values and the overall mechanical behavior evaluated from a simple analytical solution, based on the theory of linear elasticity, matched very well with those determined from the FE model, which accounted for large deformation and non-linear material behavior.

The average and standard deviation of the critical strain energy release rate G_c of PVdF/SiO_2 interface, measured from seven circular blister samples, is 2.46 ± 0.40 J m^{-2}. The XPS and SEM analysis of the fracture surfaces showed that the crack path was predominantly at the PVdF/SiO_2 interface, i.e., pure delamination, and the mechanism of failure was adhesive. Hence, the measured G_c can be considered as the energy required to break the bonds to separate PVdF from SiO_2 surfaces. Since the crack propagation occurred at the interface, fracture is mixed-mode and the measured G_c, in general, is a function of the phase angle ψ. The phase angle in the axisymmetric (circular) samples used here is 41°, hence, the $G_c = 2.46 \pm 0.40$ J m^{-2} should be associated with this phase angle. It should be noted that the G_c values reported here were measured by accounting for the residual stress in the film, but if the residual stress in the film was not measured and ignored, the error in the G_c measurement will be 7%.

Since the measured G_c is a fundamental fracture parameter that characterizes PVdF/SiO_2 interface failure, one can use $G = G_c$ as a failure criterion to predict interface failure irrespective of sample geometry, including the interfaces in a composite battery electrode. To validate and demonstrate the predictive capability of the fracture criterion $G = G_c$, rectangular (plane strain) samples with PVdF films on SiO_2 surface were tested and failure pressure was recorded. Using the measured G_c in a finite element analysis, the failure pressure of the rectangular samples was predicted successfully. The predictions agreed remarkably well, demonstrating that the critical energy release rate G_c measured is a fundamental fracture property that characterizes the PVdF/SiO_2 interface failure. This study paves the way for the implementation of fracture mechanics ideas in multiphysics battery models to simulate and predict the degradation behavior of batteries.

Supplementary Information The online version contains supplementary material available at https://doi.org/10.1007/s11340-022-00924-9.

Acknowledgements Authors would like to acknowledge funding from the National Science Foundation through grant# CMMI-1652409 and CMMI-2026717.

Declarations

Ethical Statement/Conflict of Interest Statement The authors declare that they have no potential conflicts of interest.

References

1. Scrosati B, Garche J (2010) Lithium batteries: Status, prospects and future. J Power Sources 195:2419–2430
2. Thackeray MM, Wolverton C, Isaacs ED (2012) Electrical energy storage for transportation - Approaching the limits of, and going beyond, lithium-ion batteries. Energy and Environmental Science 5:7854–7863
3. Kasavajjula U, Wang C, Appleby AJ (2007) Nano- and bulk-silicon-based insertion anodes for lithium-ion secondary cells. J Power Sources 163:1003–1039. https://doi.org/10.1016/j.jpowsour.2006.09.084
4. Rakshit S, Pakhare AS, Ruiz O et al (2020) Measurement of Volume Changes and Associated Stresses in Ge Electrodes Due to Na/Na + Redox Reactions. J Electrochem Soc C. https://doi.org/10.1149/1945-7111/abd5fc
5. Sethuraman VA, Chon MJ, Shimshak M et al (2010) In situ measurements of stress evolution in silicon thin films during electrochemical lithiation and delithiation. J Power Sources 195:5062–5066. https://doi.org/10.1016/j.jpowsour.2010.02.013
6. Mukhopadhyay A, Kali R, Badjate S et al (2014) Plastic deformation associated with phase transformations during lithiation/delithiation of Sn. Scripta Mater 92:47–50. https://doi.org/10.1016/j.scriptamat.2014.08.011
7. Rakshit S, Tripuraneni R, Nadimpalli SPV (2018) Real-Time Stress Measurement in SiO2 Thin Films during Electrochemical Lithiation/Delithiation Cycling. Exp Mech 58:537–547. https://doi.org/10.1007/s11340-017-0371-2
8. Nadimpalli SPV, Tripuraneni R, Sethuraman VA (2015) Real-Time Stress Measurements in Germanium Thin Film Electrodes during Electrochemical Lithiation/Delithiation Cycling. J Electrochem Soc 162:A2840–A2846. https://doi.org/10.1149/2.0941514jes
9. Peled E (1979) The Electrochemical Behavior of Alkali and Alkaline Earth Metals in Nonaqueous Battery Systems—The Solid Electrolyte Interphase Model. J Electrochem Soc 126:2047–2051. https://doi.org/10.1149/1.2128859
10. Nadimpalli SPV, Sethuraman VA, Dalavi S et al (2012) Quantifying capacity loss due to solid-electrolyte-interphase layer formation on silicon negative electrodes in lithium-ion batteries. J Power Sources 215:145–151. https://doi.org/10.1016/j.jpowsour.2012.05.004
11. Pinson MB, Bazant MZ (2013) Theory of SEI Formation in Rechargeable Batteries: Capacity Fade, Accelerated Aging and Lifetime Prediction. J Electrochem Soc 160:A243–A250. https://doi.org/10.1149/2.044302jes
12. Fransson L, Eriksson T, Edström K et al (2001) Influence of carbon black and binder on Li-ion batteries. J Power Sources 101:1–9. https://doi.org/10.1016/S0378-7753(01)00481-5
13. Chen Z, Christensen L, Dahn JR (2003) Comparison of PVDF and PVDF-TFE-P as Binders for Electrode Materials Showing Large Volume Changes in Lithium-Ion Batteries. J Electrochem Soc 150:A1073. https://doi.org/10.1149/1.1586922
14. Chen Z, Christensen L, Dahn JR (2003) A study of the mechanical and electrical properties of a polymer/carbon black binder system used in battery electrodes. J Appl Polym Sci 90:1891–1899. https://doi.org/10.1002/app.12863
15. Obrovac MN, Krause LJ (2007) Reversible Cycling of Crystalline Silicon Powder. J Electrochem Soc 154:A103. https://doi.org/10.1149/1.2402112
16. Li J, Lewis RB, Dahn JR (2007) Sodium Carboxymethyl Cellulose. Electrochem Solid-State Lett 10:A17. https://doi.org/10.1149/1.2398725
17. Mazouzi D, Karkar Z, Hernandez CR et al (2015) Critical roles of binders and formulation at multiscales of silicon-based composite electrodes. J Power Sources 280:533–549. https://doi.org/10.1016/j.jpowsour.2015.01.140
18. Ryu JH, Kim JW, Sung Y-E, Oh SM (2004) Failure Modes of Silicon Powder Negative Electrode in Lithium Secondary Batteries. Electrochem Solid-State Lett 7:A306. https://doi.org/10.1149/1.1792242
19. Mazouzi D, Lestriez B, Roué L, Guyomard D (2009) Silicon composite electrode with high capacity and long cycle life. Electrochem Solid-State Lett 12:A215. https://doi.org/10.1149/1.3212894
20. Yoo M, Frank CW, Mori S, Yamaguchi S (2004) Interaction of poly(vinylidene fluoride) with graphite particles. 2. Effect of solvent evaporation kinetics and chemical properties of PVDF on the surface morphology of a composite film and its relation to electrochemical performance. Chem Mater 16:1945–1953. https://doi.org/10.1021/cm0304593
21. Chen L, Xie X, Xie J et al (2006) Binder effect on cycling performance of silicon/carbon composite anodes for lithium ion batteries. J Appl Electrochem 36:1099–1104. https://doi.org/10.1007/s10800-006-9191-2
22. Rahani EK, Shenoy VB (2013) Role of Plastic Deformation of Binder on Stress Evolution during Charging and Discharging in Lithium-Ion Battery Negative Electrodes. J Electrochem Soc 160:A1153–A1162. https://doi.org/10.1149/2.046308jes
23. Nadimpalli SPV, Sethuraman VA, Abraham DP et al (2015) Stress Evolution in Lithium-Ion Composite Electrodes during Electrochemical Cycling and Resulting Internal Pressures on the Cell Casing. J Electrochem Soc 162:A2656–A2663. https://doi.org/10.1149/2.0341514jes
24. Santimetaneedol A, Tripuraneni R, Chester SA, Nadimpalli SPV (2016) Time-dependent deformation behavior of polyvinylidene fluoride binder: Implications on the mechanics of composite electrodes. J Power Sources 332:118–128. https://doi.org/10.1016/j.jpowsour.2016.09.102
25. Singh G, Bhandakkar TK (2017) Analytical Investigation of Binder's Role on the Diffusion Induced Stresses in Lithium Ion Battery through a Representative System of Spherical Isolated Electrode Particle Enclosed by Binder. J Electrochem Soc 164:A608–A621. https://doi.org/10.1149/2.0361704jes
26. Sethuraman VA, Nguyen A, Chon MJ et al (2013) Stress Evolution in Composite Silicon Electrodes during Lithiation/Delithiation. J Electrochem Soc 160:A739–A746. https://doi.org/10.1149/2.021306jes
27. Chen J, Liu J, Qi Y et al (2013) Unveiling the Roles of Binder in the Mechanical Integrity of Electrodes for Lithium-Ion Batteries. J Electrochem Soc 160:A1502–A1509. https://doi.org/10.1149/2.088309jes
28. Kierzek K (2016) Influence of Binder Adhesion Ability on the Performance of Silicon/Carbon Composite as Li-Ion Battery Anode. J Mater Eng Perform 25:2326–2330. https://doi.org/10.1007/s11665-016-2083-7
29. Yoo M, Frank CW, Mori S, Yamaguchi S (2003) Effect of poly(vinylidene fluoride) binder crystallinity and graphite

structure on the mechanical strength of the composite anode in a lithium ion battery. Polymer 44:4197–4204. https://doi.org/10.1016/S0032-3861(03)00364-1
30. Chen Z, Christensen L, Dahn JR (2003) Large-volume-change electrodes for Li-ion batteries of amorphous alloy particles held by elastomeric tethers. Electrochem Commun 5:919–923. https://doi.org/10.1016/j.elecom.2003.08.017
31. Ebner M, Marone F, Stampanoni M, Wood V (2013) Visualization and Quantification of Electrochemical and Mechanical Degradation in Li Ion Batteries. Science 342:716–720. https://doi.org/10.1126/science.1241882
32. Müller S, Wood V, Baade P et al (2018) Quantification and modeling of mechanical degradation in lithium-ion batteries based on nanoscale imaging. Nat Commun 9:2340. https://doi.org/10.1038/s41467-018-04477-1
33. Pharr M, Suo Z, Vlassak JJ (2013) Measurements of the fracture energy of lithiated silicon electrodes of Li-Ion batteries. Nano Lett 13:5570–5577. https://doi.org/10.1021/nl403197m
34. Al-Obeidi A, Kramer D, Thompson CV, Mönig R (2015) Mechanical stresses and morphology evolution in germanium thin film electrodes during lithiation and delithiation. J Power Sources 297:472–480. https://doi.org/10.1016/j.jpowsour.2015.06.155
35. Hohlfelder RJ (1999) Bulge and Blister Testing of Thin Films and Their Interfaces
36. Xiang Y, Chen X, Vlassak JJ (2005) Plane-strain Bulge Test for Thin Films. J Mater Res 20:2360–2370. https://doi.org/10.1557/jmr.2005.0313
37. Cao Z, Wang P, Gao W et al (2014) A blister test for interfacial adhesion of large-scale transferred graphene. Carbon 69:390–400. https://doi.org/10.1016/j.carbon.2013.12.041
38. Cao Z, Tao L, Akinwande D et al (2016) Mixed-mode traction-separation relations between graphene and copper by blister tests. Int J Solids Struct 84:147–159. https://doi.org/10.1016/j.ijsolstr.2016.01.023
39. MATLAB Documentation. https://www.mathworks.com/help/matlab/. Accessed 17 Jan 2022
40. Hibbit KS, Karlsson B (2005) ABAQUS reference manuals. Dassault Systemes
41. Freund LB, Suresh S (2004) Thin Film Materials. Cambridge University Press
42. Kanninen MF, Popelar CH (1985) Advanced Fracture Mechanics (Oxford Engineering Science Series)
43. Anderson TL (2017) Fracture Mechanics: Fundamentals and Applications, 3rd edn. CRC Press
44. Raju IS (1987) Simple Formulas for Strain Energy Release Rates with Higher Order and Singular Finite Elements. Calculation of strain-energy release rates with higher order and singular finite elements
45. Figiel Ł, Lauke B (2006) Interface fracture of polymer films: Blister test experiments and modelling. Int J Fract 139:71–89. https://doi.org/10.1007/s10704-006-6999-z
46. Hopcroft MA, Nix WD, Kenny TW (2010) What is the Young's modulus of silicon? J Microelectromech Syst 19:229–238. https://doi.org/10.1109/JMEMS.2009.2039697
47. Small MK, Nix WD (1992) Analysis of the accuracy of the bulge test in determining the mechanical properties of thin films. J Mater Res 7:1553–1563. https://doi.org/10.1557/JMR.1992.1553
48. Small MK, Daniels BJ, Clemens BM, Nix WD (1994) The elastic biaxial modulus of Ag-Pd multilayered thin films measured using the bulge test. J Mater Res 9:25–30. https://doi.org/10.1557/JMR.1994.0025
49. Ziebart V, Paul O, Baltes H (1999) Strongly buckled square micromachined membranes. J Microelectromech Syst 8:423–432. https://doi.org/10.1109/84.809057
50. Jensen HM, Thouless MD (1993) Effects of residual stresses in the blister test. Int J Solids Struct 30:779–795. https://doi.org/10.1016/0020-7683(93)90040-E
51. Thouless MD, Jensen HM (1994) The effect of residual stresses on adhesion measurements. J Adhes Sci Technol 8:579–586. https://doi.org/10.1163/156856194X00357
52. Hutchinson JW, Suo Z (1991) Mixed Mode Cracking in Layered Materials. 63–191
53. Liechti KM, Chai YS (1992) Asymmetric shielding in interfacial fracture under in-plane shear. J Appl Mech Trans ASME 59:295–304. https://doi.org/10.1115/1.2899520
54. Swadener JG, Liechti KM, Lozanne ALD (1999) The intrinsic toughness and adhesion mechanisms of a glass/epoxy interface. J Mech Phys Solids 47:223–258. https://doi.org/10.1016/S0022-5096(98)00084-2
55. Agrawal A, Karlsson AM (2006) Obtaining mode mixity for a bimaterial interface crack using the virtual crack closure technique. Int J Fract 141:75–98. https://doi.org/10.1007/s10704-006-0069-4